SCIENCE CHINA
Physics, Mechanics & Astronomy

• Article •

October 2026 Vol. 69 No. 10: 106112
https://doi.org/10.1007/s11433-026-3041-4

Critical hydrogen contents enable giant magnetocaloric effect and brittle-to-ductile transition in amorphous nanocomposites

Cheng Chen[1], Qianzi Yang[1], Qiang Luo[1*], Fan Hu[1], Mingjie Zhang[1], Mingqiang Zhang[1], Yao Zhang[1], Qianqian Wang[1], Shuangxi Song[2*], Zhijun Guo[1*], and Baolong Shen[1*]

[1] *School of Materials Science and Engineering, Jiangsu Key Laboratory of Advanced Metallic Materials, Southeast University, Nanjing 211189, China*

[2] *Shanghai Key Laboratory of Hydrogen Science & Center of Hydrogen Science, School of Materials Science and Engineering, Shanghai Jiao Tong University, Shanghai 200240, China*

Received March 10, 2026; accepted June 10, 2026; published online August 26, 2026

The development of magnetocaloric materials is fundamentally constrained by the need to simultaneously achieve a giant magnetocaloric effect (MCE) and mechanical toughness. Here, we show that this bottleneck is overcome by treating hydrogen as a microstructural tuning parameter in a Gd-based amorphous alloy (AMA). Through controlled hydrogenation, we observe small 1-2 nm GdH_2 clusters progressively evolving into a network of 2-5 nm nanocrystals. This engineered microstructure tailors the elastic modulus distribution, transforms magnetic transition behavior, and modifies the underlying critical dynamics. Notably, two distinct hydrogen concentration thresholds govern variations in mechanical and magnetocaloric performance. The brittle-to-ductile transition occurs at 0.83 wt.% hydrogen. At this point, a critical density of GdH_2 nanoclusters enables the formation of a connected shear transformation zone network and facilitates synergistic deformation between the nanoclusters and the amorphous matrix. In contrast, the giant MCE emerges only above 1.38 wt.% hydrogen, when a continuous antiferromagnetic GdH_2 skeleton forms and suppresses long-range ferromagnetic exchange. The critical window ($\geqslant$ 1.38 wt.% hydrogen) thus delivers an unprecedented combination of giant MCE ($\geqslant$ 16.14 J kg^{-1} K^{-1} at 5 T) and large plastic strain ($>$ 40%), thereby overcoming the challenge of achieving both concurrently. Our work establishes hydrogen-mediated nanocrystal engineering as a paradigm for designing high-performance nanocomposites.

hydrogenation, giant magnetocaloric effect, brittle-to-ductile transition

Citation: C. Chen, Q. Yang, Q. Luo, F. Hu, M. Zhang, M. Zhang, Y. Zhang, Q. Wang, S. Song, Z. Guo, and B. Shen, Critical hydrogen contents enable giant magnetocaloric effect and brittle-to-ductile transition in amorphous nanocomposites, Sci. China-Phys. Mech. Astron. **69**, 106112 (2026), https://doi.org/10.1007/s11433-026-3041-4

1 Introduction

The global increase in energy demand and the rising need for sustainable cooling have propelled magnetic refrigeration (MR) to the forefront of alternative cooling technology. As an energy-efficient and environmentally friendly solid-state method, MR operates on the MCE, which is the intrinsic thermal response of magnetic materials to a changing magnetic field [1]. The practical implementation and scalability of MR systems critically depend on the development of advanced magnetocaloric materials, which need a delicate balance between outstanding magnetocaloric performance and exceptional mechanical robustness. The former requires a giant magnetic entropy change ($-\Delta S_M$) with minimal

*Corresponding authors (Qiang Luo, email: q.luo@seu.edu.cn; Shuangxi Song, email: songshuangxi@sjtu.edu.cn; Zhijun Guo, email: zj-guo@seu.edu.cn; Baolong Shen, email: blshen@seu.edu.cn)

© Science China Press 2026

magnetic hysteresis, while the latter is essential for ensuring long-term reliability and cyclability under repeated thermal and magnetic cycling in practical applications. Attaining this synergy remains a long-standing challenge within the field.

Typical crystalline magnetocaloric materials, such as Gd(Si,Ge) [2], La(Fe,Si) [3,4], MnFe(P,As) [5], and Ni-Mn-based alloys [6], exhibit a giant MCE near their magnetic transition temperature (T_M). This effect originates from a first-order magnetic phase transition (FOPT) driven by strong magneto-structural coupling. However, the FOPT is often accompanied by significant thermal and magnetic hysteresis. Furthermore, the abrupt volume changes produce large internal stress (which can exceed the fracture toughness of the refrigerants) [7,8]. Consequently, these materials are prone to energy losses, microcracking, and progressive pulverization, which deteriorate both the efficiency and long-term integrity of practical MR systems [9]. To mitigate these challenges, composite strategies have been employed in crystalline magnetocaloric materials (such as the La(Fe,Si) system), including *in-situ* formation of a secondary phase [3,4] or *ex-situ* bonding of the crystalline matrix to toughening phases such as metals or polymers [10-13]. Nevertheless, these secondary phases severely dilute the $-\Delta S_M$, while providing only limited mechanical enhancement.

In contrast, AMAs present several advantages for magnetocaloric applications, including high strength, excellent corrosion resistance, and magnetic softness, all originating from their fully disordered atomic structure [14,15]. However, they typically exhibit a substantially lower MCE than crystalline candidates and suffer from inherent brittleness driven by strain localization in shear bands [16-20]. To improve the MCE, precise compositional tuning, such as substituting rare-earth elements or introducing minor alloying elements, has been utilized to develop AMAs with excellent magnetocaloric properties [21,22]. Meanwhile, conventional composite strategies, such as *in-situ* amorphous/crystalline dual-phase design or post-treatments partial induced nanocrystallization (e.g., current annealing), have been widely employed to enhance magnetocaloric performance [23-28]. Although these composite approaches may improve the refrigerant capacity (RC) at the expense of the maximum $-\Delta S_M$ ($-\Delta S_M^{pk}$) and adjust the T_M, they do not mitigate the inherent brittleness. Recently, hydrogenation was found to trigger the homogeneous precipitation of nano-sized ordered hydrides (NOH) within a stable glassy matrix of a Gd-based AMA, thereby enhancing both magnetocaloric and mechanical properties [29]. Nevertheless, the underlying synergistic mechanism between hydrides and the amorphous matrix, as well as their precise dependence on hydrogen concentration, remains elusive. Compounding the uncertainty, it has been reported that the effect of hydrogenation on MCE of AMAs varies across compositions, increasing it in some systems and reducing it in others [18,29-31]. Accordingly, it is imperative to establish a clear structure-property relationship that directly correlates hydrogen content with the microstructure, magnetocaloric, and micromechanical properties for targeted performance optimization.

This study explores the evolution of microstructure, magnetocaloric and mechanical properties of the $Gd_{55}Co_{17.5}Al_{27.5}$ AMA induced by controlled hydrogenation. Two distinct critical thresholds in hydrogen content dependence of MCE and mechanical performances are identified, where a significant increase in $-\Delta S_M$ from 9.14 to 16.14 J kg^{-1} K^{-1} occurs at ~ 1.38 wt.% H and a remarkable improvement in compressive plastic strain (from ~15% to over 40%) emerges at ~ 0.83 wt.% H. The sequential attainment of these dual thresholds delineates an optimal hydrogen content window ($\geqslant$ 1.38 wt.%) that breaks the bottleneck preventing the coexistence of a giant magnetocaloric effect and large plasticity. It is revealed that the mechanical threshold is at 0.83 wt.% H is triggered by a high density of 2-5 nm hydride clusters that promote cooperative shear-transformation-zone (STZ) nucleation and profuse shear banding. Conversely, the threshold at 1.38 wt.% H coincides with magnetic percolation, as a continuous antiferromagnetic hydride skeleton emerges to suppress long-range ferromagnetic order, giving rise to the giant MCE. This work offers fundamental insights and a design paradigm for next-generation magnetocaloric materials.

2 Experimental methods

The $Gd_{55}Co_{17.5}Al_{27.5}$ alloy was prepared by arc-melting pure Gd (99.9 wt.%), Co (99.99 wt.%), and Al (99.99 wt.%) elements. To prevent oxidation, both melting and subsequent gas atomization (8 MPa argon) were conducted in chambers pre-evacuated to $< 1\times10^{-3}$ Pa. The resulting amorphous powders were handled exclusively in an argon-filled glove box and stored under vacuum. Powders with particle sizes of 25-30 μm were sieved for isothermal hydrogenation. After thoroughly evacuating the reactor, samples with hydrogen contents of 0, 0.39, 0.83, 1.38, and 1.51 wt.% were obtained by varying the hydrogenation time.

The structure of hydrogenated powders was characterized using X-ray diffraction (XRD, Bruker D8 Discover). Their thermal properties were evaluated using a differential scanning calorimeter (DSC, Netzsch 404 F3) at 20 K/min under argon flow. The morphology was characterized by scanning electron microscopy (SEM, Thermo Fisher Verios 5UC). Furthermore, nanoscale structural features were examined by a spherical aberration-corrected transmission electron microscope (TEM, Thermo Fisher Spectra 300), with specimens prepared via focused ion beam (FIB, Thermo Fisher

Helios 5UX). To avoid potential influence of the thin native oxide layer on the powder surface, our TEM characterization was performed specifically on the interior regions of the powder particles.

Magnetic properties were characterized using a SQUID magnetometer (MPMS, Quantum Design) for DC magnetization and a physical properties measurement system (PPMS, Quantum Design) for AC susceptibility measurements. Using the MPMS, temperature-dependent magnetization under both zero-field-cooling (ZFC) and field-cooling (FC) conditions was measured from 2 to 200 K under an applied magnetic field of 0.01 T, after cooling the sample to 2 K. Magnetization hysteresis loops were recorded at 5 K. Isothermal magnetization curves (*M*-*H*) were acquired at different temperatures between 2 and 180 K by sweeping the field from 0 to 5 T. AC susceptibility was measured on the PPMS at 13 to 9673 Hz with a 5 Oe oscillating field.

Mechanical properties were assessed via nanoindentation and micro-compression testing. Nanoscale mechanical testing was conducted on the powders using a NanoTest Vantage (Micro Materials Ltd) equipped with a standard Berkovich diamond indenter. Atomic force microscopy (AFM, Bruker) was employed to analyze the modulus distribution on an area of 1 μm × 1 μm. Micropillars were fabricated from individual powder particles using FIB. Micro-compression tests were performed at room temperature using a nanoindenter (Bruker TI980) under a constant displacement rate (nominal strain rate: 5×10^{-3} s^{-1}). Five pillars were tested for each condition to ensure statistical reliability.

3 Results and discussion

3.1 Hydrogenation and microstructure analysis

As shown in the inset SEM image in Supporting Information Figure S1, the gas-atomized Gd-based AMA powders exhibit a spherical morphology and a relatively uniform size distribution. The corresponding hydrogen absorption kinetics, depicted in the main panel of Supporting Information Figure S1 as hydrogen content versus time, reveal the rate and capacity of hydrogen uptake by the alloy. The absorption curve exhibits a two-stage hydrogenation behavior, an initial rapid uptake (0-10 h) followed by gradual saturation, stabilizing at 1.51 wt.% H. Five samples, labeled H0-H4, were prepared at increasing absorbed-hydrogen levels (see Supporting Information Table S1) to cover the entire hydrogenation path. These specimens underpin a systematic investigation of how hydrogen content governs microstructural evolution, MCE, and mechanical properties. The XRD patterns of all H0-H4 powders (see Supporting Information Figure S2(a)) exhibit diffuse scattering halos without any detectable Bragg peaks, confirming the existence of an amorphous phase (within the detection limit of XRD). The main diffuse halo shifts to a lower angle with increasing H content, indicating an expansion of the average atomic spacing [32-34]. DSC traces (see Supporting Information Figure S2(b)) reveal that hydrogenation alters the thermal transition sequence through competing processes of crystallization of the amorphous matrix, growth of GdH_2 nanocrystals, and hydride decomposition. The hydrogen-free H0 alloy shows a single exothermic peak corresponding to the crystallization of the glassy phase. Upon hydrogenation, H1 (0.39 wt.% H) and H2 (0.83 wt.% H) exhibit two exothermic events, the first attributed to GdH_2 growth and the second to matrix crystallization [35]. In H2, hydride decomposition appears as an endothermic contribution that weakens and reshapes the first exothermic peak. At higher hydrogen levels (H3 at 1.38 wt.% H and H4 at 1.51 wt.% H), GdH_2 growth ceases, and a broad endothermic peak dominates, indicating that hydride decomposition becomes the primary thermal process.

The high-angle annular dark-field scanning transmission electron microscopy (HAADF-STEM) and aberration-corrected high-resolution TEM (HRTEM) were further employed to probe the local structure of the H0-H4 samples. The combined HAADF-STEM uniformity (Figure 1(a1)) and HRTEM maze-like contrast (Figure 1(a2)) in the H0 sample corroborate a fully amorphous structure without nanoscale crystallinity or phase separation. After hydrogenation, the H1 sample shows the initial formation of 1-2 nm ordered nanoclusters, identified as NOHs by bright HAADF-STEM spots and HRTEM lattice fringes (see Supporting Information Figure S3(a) and (b)). As hydrogen content increases in H2, the density of these nanoclusters rises (Figure 1(b1) and (b2)). In the H3 sample, the nanocrystals grow to 2-5 nm, and their population density increases further, as confirmed by both imaging techniques (Figure 1(c1) and (c2)). Besides, the selected area electron diffraction (SAED) patterns for H1, H2, and H3 (insets in Figure 1(b2) and (c2); Supporting Information Figure S3(b)) all exhibit a broad diffuse halo similar to that of the fully amorphous H0 sample (inset of Figure 1(a2)). The absence of resolvable Bragg reflections indicates that the amorphous matrix remains dominant, with the nanocrystal volume fraction below the detection limit of selected-area diffraction. In contrast, H4 exhibits a high density of 2-5 nm NOHs in HAADF-STEM (Figure 1(d1)) and HRTEM (Figure 1(d2)), and its SAED pattern displays sharp diffraction rings (inset Figure 1(d2)) corresponding to the polycrystalline GdH_2. To further quantify the evolution of medium-range ordered domains during hydrogenation, we applied autocorrelation transform analysis to the HRTEM images in the yellow-framed regions of Figure 1(a2)-(d2) and Supporting Information Figure S3 (b). The resulting maps in Figure 1(a3)-(d3) and Supporting Information Figure S3(c) enclose crystal-like ordering (CLO) domains (both GdH_2 nanocrystals and CLO clusters

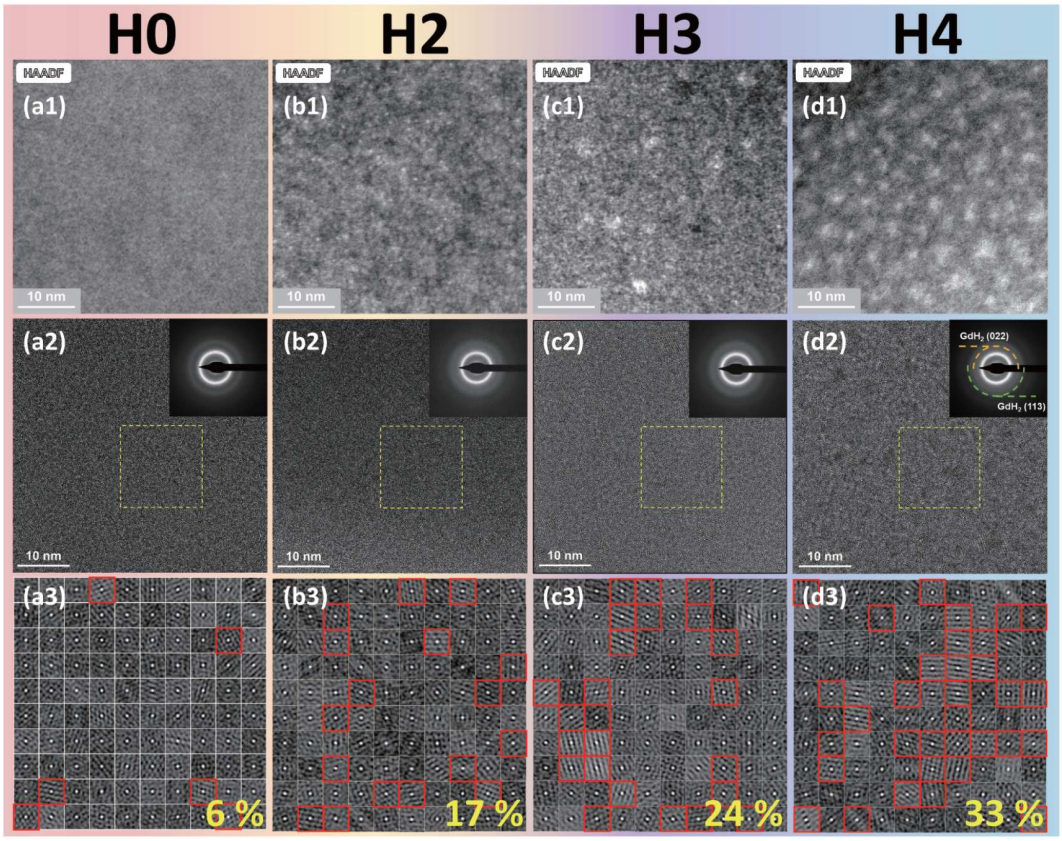

Figure 1 (Color online) Microstructural characterization of the Hx samples. (a1)-(d1) HAADF-TEM image of H0, H2, H3 and H4. (a2)-(d2) HRTEM images with insets showing the corresponding SAED patterns. (a3)-(d3) Autocorrelation function analysis of the yellow-framed regions indicated in (a2)-(d2).

within the glassy matrix) in red frames. The areal fraction of these CLO regions rises systematically from 6% (H0) to 33% (H4). These observations trace a continuous evolution from nucleation and growth to the final formation of an interconnected network of GdH_2 nanocrystals. This demonstrates that hydrogen content serves as a quantitative parameter for engineering the nanoscale architecture of glass-hydride composites.

3.2 Magnetocaloric performances

Figure 2(a) presents the temperature dependence of the ZFC and FC magnetization at 0.01 T for the H0-H4 samples. It is evident that the T_M of the hydrogenated samples progressively decreases with increasing volume fraction of GdH_2 nanocrystalline phases. The Curie-Weiss temperature (inset) changes gradually from 107 K for H0 to −27 K for H4, signaling a crossover from a ferromagnetic to an antiferromagnetic dominant exchange interaction with increasing hydrogen content. The resulting antiferromagnetic order of H1-H4 samples is also corroborated by the low-temperature divergence between ZFC and FC curves and by the frequency-independent T_M derived from the real part of the AC susceptibility (see Supporting Information Figure S4). Figure 2(b) displays the *M-H* curves for the five samples at 25 K. The slope of the curves in the low-field region decreases gradually with increasing volume fraction of the antiferromagnetic GdH_2 phase. This observation is consistent with the rapid decrease in the maximum magnetization value with increasing hydrogen content (Figure 2(a)).

Based on the isothermal magnetization curves (see Supporting Information Figure S5), the $-\Delta S_M$ of the five samples can be calculated using the Maxwell relations. Figure 2 (c) and (d) show the hydrogen concentration dependence of the magnetocaloric response in the present samples. With increasing hydrogen content, the $-\Delta S_M$ curves systematically shift to lower temperature and become sharper. Specifically, the $-\Delta S_M^{pk}$ falls from 9.14 J kg^{-1} K^{-1} at 97 K for the hydrogen-free H0 sample to 6.73 J kg^{-1} K^{-1} at 76 K for H1 and 6.84 J kg^{-1} K^{-1} at 29 K for H2 (Figure 2(c)), signaling a progressive dilution of ferromagnetic exchange interaction. In the dilute regime (H1 and H2), only a portion of the Gd atoms is converted into nanoscale GdH_2 clusters, resulting in a dual-phase (glass and hydride phases) microstructure, where ~1-2 nm GdH_2 clusters are embedded in a Gd-depleted, still-ferromagnetic Al/Co-rich amorphous matrix. The reduced density of exchange-coupled Gd moments

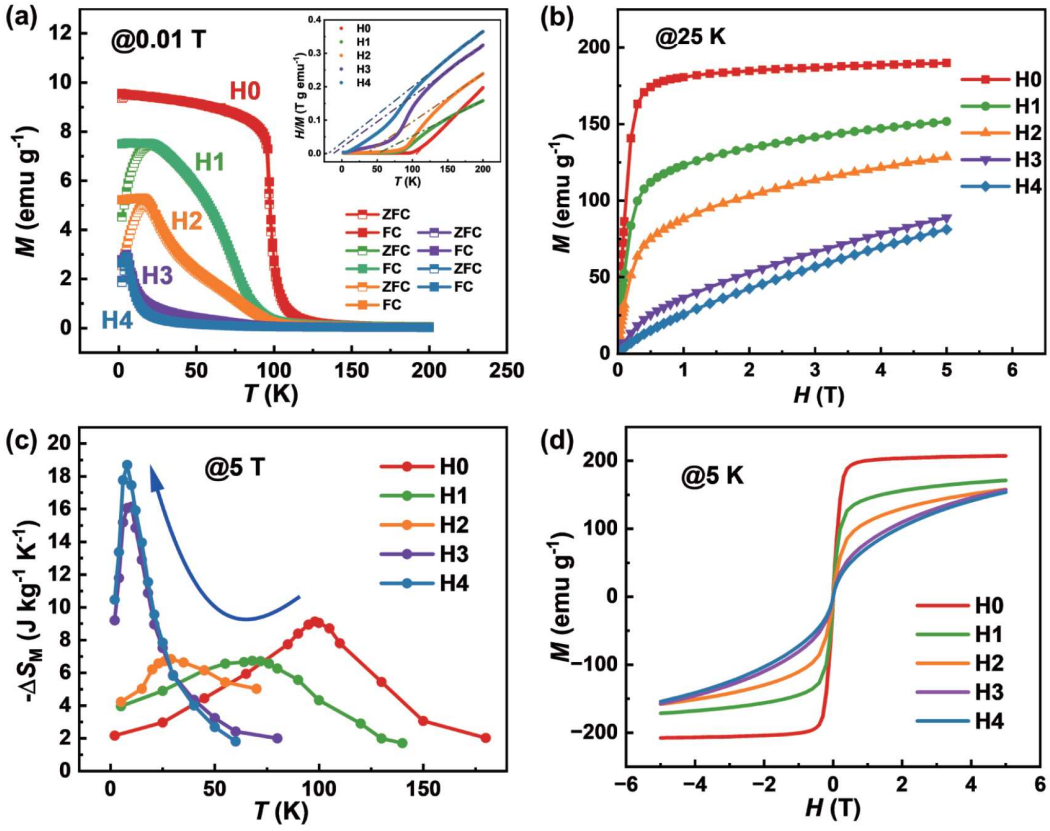

Figure 2 (Color online) Magnetic properties of the H0-H4 samples. (a) Temperature dependence of magnetization curves. The inset shows the corresponding Curie-Weiss fits in the paramagnetic region. (b) Isothermal magnetization curves measured at 25 K. (c) $-\Delta S_{\mathrm{M}}$ as a function of temperature under a magnetic field change of 5 T. (d) Magnetic hysteresis loops recorded at 5 K within an applied field range of ±5 T.

lowers the T_{M} and suppresses $-\Delta S_M^{pk}$ to ~6.8 J kg^{-1} K^{-1} near 30 K. When the hydrogen content approaches saturation (H3-H4), nearly all Gd is incorporated into the GdH_2 phase. As a result, the primary origin of the magnetocaloric response shifts to the antiferromagnetic GdH_2 network. This network substantially suppresses the long-range ferromagnetic exchange of the original matrix, leaving behind only residual and significantly weakened ferromagnetic correlations in the confined amorphous regions [36]. Consequently, T_{M} collapses to ~7 K while $-\Delta S_M^{pk}$ ultimately rises to 18.7 J kg^{-1} K^{-1} (a ~105% increase relative to H0). This enhancement agrees with two earlier reports. Mathew et al. [37] showed that in GdH_2 nanocrystals, the grain size affects both the magnitude and the shape of the $-\Delta S_{\mathrm{M}}$ peak. Here, as the GdH_2 grains grow from 1-2 nm (H1 and H2) to 2-5 nm (H3 and H4), the peak becomes sharper and the magnitude larger, consistent with their finding. Liu et al. [38] further reported that in rare-earth Laves phases, the magnetic entropy change increases as the Curie temperature decreases. Our H3 and H4 samples, with their T_{M} shifted to lower temperatures than H1 and H2, follow the same trend. Note that the MCE performance of H3 and H4 surpasses that of most AMAs and is comparable to the best-reported amorphous composites [16-18,24,31,39]; their distinct advantage lies in the far superior mechanical properties (high yield strength and large plasticity), which are critical for practical applications. Furthermore, unlike many crystalline materials exhibiting coupled giant MCE with significant thermal or magnetic hysteresis, all hydrogenated samples retain excellent soft magnetic properties (Figure 2(d)). This excellent soft magnetic performance ensures low energy losses during cooling cycles, thereby enhancing their efficiency and reversibility as magnetocaloric refrigerants.

To reveal the impact of hydrogenation on magnetic transition in H0-H4 samples, critical behavior near T_{M} was analyzed. First, the magnetic phase transition type was identified by constructing Arrott plots (M^2 *vs.* H/M) at various temperatures (see Supporting Information Figure S6). The positive slope observed in the Arrott plots near T_{M} indicates a second-order magnetic phase transition for all samples according to Banerjee's criterion [40]. The critical exponents β, γ, and δ, derived from the universal scaling hypothesis to describe the spontaneous magnetization M_{S}

(T), initial susceptibility χ_0 (T), and M-H isotherm at T_M, respectively, can be defined as follows [41-43]:

$$M_S(T) = M_0(-\varepsilon)^{\beta} \quad \varepsilon < 0, \text{below} \quad T_C, \tag{1}$$

$$\chi_0^{-1}(T) = (h_0 / M_0)\varepsilon^{\gamma} \quad \varepsilon > 0, \text{ above } T_C, \tag{2}$$

$$M = D\mu_0 H^{1/\delta} \quad \varepsilon = 0, \text{at } T_C, \tag{3}$$

where $\varepsilon = (T - T_C) / T_C$ is the reduced temperature, and h_0/M_0 and D are the critical amplitudes. The critical scaling $M = D\mu_0 H^{1/\delta}$ analysis reveals fundamentally distinct critical behaviors between H0 and H4, as evidenced by their respective critical exponents. H0 (with β = 0.430, γ = 1.101, and δ = 3.374) is close to the 3D Heisenberg model [44], while H4 (with β = 0.497, γ = 0.906, and δ = 2.951) follows the mean field model (see Suppporting Information Figures S7, S8, and Table S2), suggesting that hydrogenation modifies the range and nature of the magnetic interactions within the system. The findings for H0 indicate that short-range interactions are critical in determining the magnetic characteristics [45]. In contrast, H4 establishes a magnetic landscape characterized by competing antiferromagnetic order and weak ferromagnetic interactions, with super-exchange AFM coupling [46]. Moreover, due to the structural and chemical heterogeneity of the H1-H3 samples, the critical behavior analysis was not performed.

3.3 Mechanical properties

Next, we examine the effect of dual-phase architecture on the local mechanical heterogeneity of the H0-H4 samples by using AFM in Peak Force Quantitative Nanomechanical Mapping mode. This enabled us to correlate nanoscale modulus variations with the precipitation evolution of GdH_2 nanocrystals. The corresponding statistical distribution curves of $\Delta E_r / E_r^p$ for the H0-H4 samples are shown in Figure 3 and Supporting Information Figure S9, and all curves can be fitted very well by a Gaussian function. The evolution of the modulus distribution is consistent with the microstructural evolution shown in Figure 1 and Supporting Information Figure S3. The H0 sample exhibits a single broad peak of modulus distribution (Figure 3(a)), characteristic of a fully amorphous Gd-Co-Al matrix. Early nucleation of ~1-2 nm GdH_2 clusters (H1 and H2) introduces a low-modulus phase, resulting in a distinct bimodal modulus distribution (Figure 3(b) and (c)). The growing intensity of the low-modulus peak mirrors the increasing population of these soft nanocrystals, while the broadest distribution curve of H2 indicates its maximum microstructural heterogeneity [47]. Further hydrogenation to H3-H4 yields a modified bimodal pattern characterized by a shallow valley and reduced peak separation (Figure 3(d) and (e)). This evolution corresponds to the stiffening of the now larger (2-5 nm) GdH_2 nanocrystals and a concurrent slight softening of the glassy matrix, due to hydrogen-induced lattice expansion [29]. The evolution of mechanical heterogeneity can be further quantified at both nano- and micro-scales, as shown in Figures 3(f) and 4. The full width at half maximum (FWHM) of the

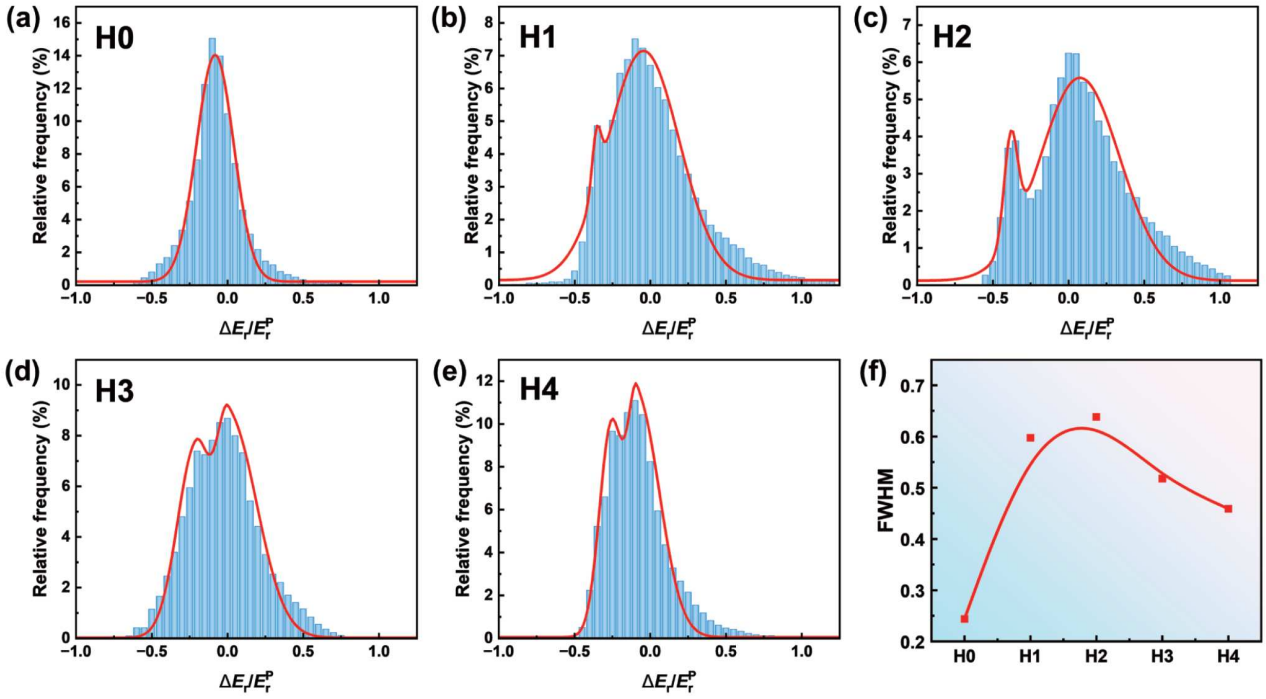

Figure 3 (Color online) Nanoindentation mapping and statistical distribution analysis. (a)-(e) Statistical analysis based on the normalized distribution curves ($\Delta E_r / E_r^p$) for the H0, H1, H2, H3 and H4 samples. (f) Full width at half maximum extracted from the $\Delta E_r / E_r^p$ curves for all samples (H0-H4).

$\Delta E_r / E_r^p$ distributioncurve peaks at H2, reflecting maximal heterogeneity in the nanoscale elastic modulus. The load-displacement (*P-h*) curves from nanoindentation tests (Figure 4) further reveal a distinct evolution in mechanical heterogeneity with hydrogenation. Compared with the H0 sample (Figure 4(a) and (f)), the H1 and H2 specimens display markedly increased scatter in hardness and reduced elastic modulus across multiple indent locations (Figure 4(b), (c), and (f)). This broadening reflects a significant rise in micro-scale mechanical heterogeneity, consistent with the composite structure of soft GdH_2 nanoclusters dispersed in a rigid amorphous matrix. Such heterogeneity peaks in the H2 and H3 samples, as indicated by the maximum statistical spread in measured properties (Figure 4). This enhanced mechanical heterogeneity at different length scales balances the need for distributed plasticity carriers with effective resistance to catastrophic shear banding, directly contributing to the suppression of intrinsic brittleness in the AMA.

To clarify how hydrogen content affects the mechanical deformation behavior, we carried out micro-compression tests on micro-pillars (H0-H4) and used SEM to image the surface. As indicated in Figure 5, the engineering stress-strain curves, corrected using the micro-pillar Young's modulus formula [48], exhibit a pronounced transition in mechanical response with increasing hydrogen content. The H0 and H1 samples with no or low hydrogen content demonstrated relatively low yield strengths (1.2-1.6 GPa) and limited compressive plasticity (~15%). In contrast, the H2-H4 samples with higher hydrogen content achieved notably higher strength and larger plasticity, with yield stresses around 2 GPa, plastic strains exceeding 40% for H2, and surpassing 50% for H3 and H4. Notably, the H4 and hydrogen-saturated samples in the previous study [29] possess the identical composition, and therefore both exhibit this combination of high strength and large plasticity. The numerical differences observed in their yield strength and plastic strain are entirely attributed to the sample size effect (1 μm vs. 500 nm pillar diameter). To systematically elucidate the intrinsic correlation among hydrogen content, microstructure, and properties, a combined structural and property evolution is presented in Figure 6. As shown in Figure 6(a), the microstructure evolves through three distinct stages with increasing hydrogen content: from a fully amorphous state (H0), to isolated GdH_2 nanoclusters embedded in an amorphous glass matrix (H1 and H2), to an interconnected dual-phase nanohydride network (H3 and H4). This structural evolution governs two critical performance thresholds. The first threshold occurs around H2 (0.83 wt.% H), where the formation of isolated GdH_2 nanoclusters provides sufficient heterogeneous interfaces to promote extensive shear band multiplication. This leads to the brittle-to-ductile transition observed in Figure 6(b), with a significant increase in compressive strain while maintaining the high yield strength. The second threshold appears around H3 (1.38 wt.% H), where the nanohydride clusters interconnect into a continuous network. This network acts as a robust antiferromagnetic skeleton, which dramatically enhances the magnetocaloric effect (Figure 6(c)). The giant $-\Delta S_M$ emer-

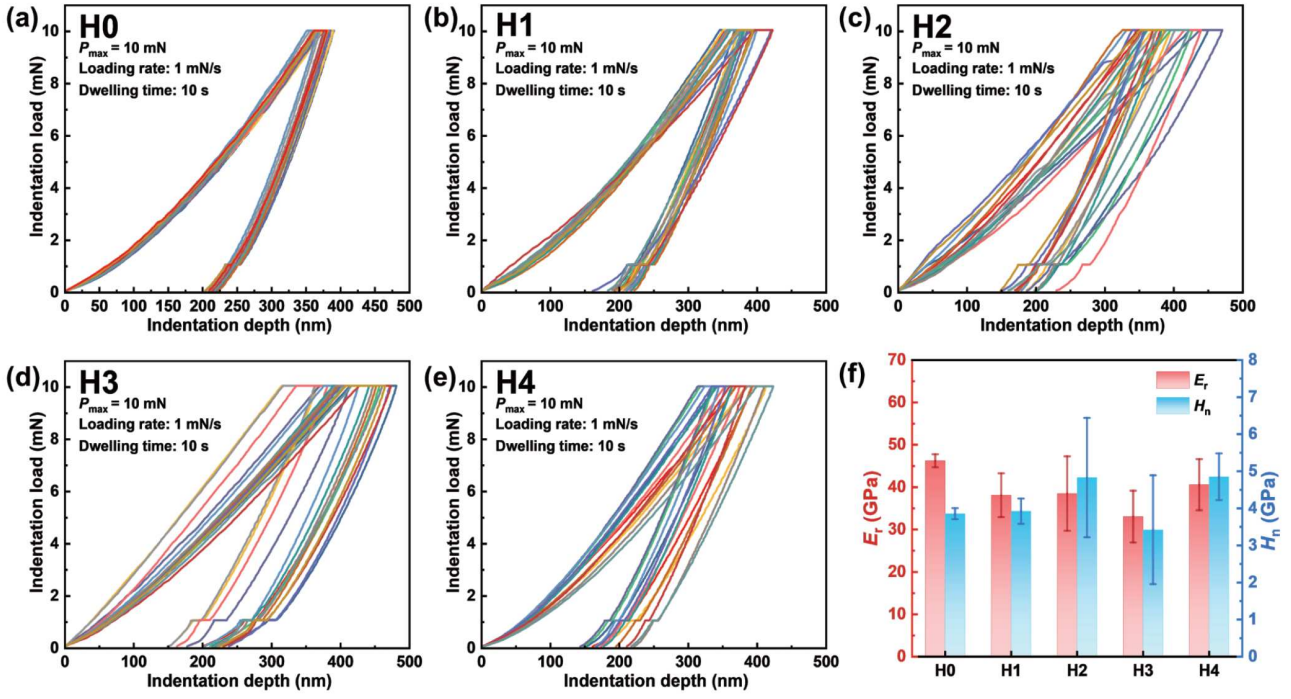

Figure 4 (Color online) Nanoindentation response. (a)-(e) Load-depth curves for the H0-H4 samples. (f) Variation of the hardness (H_n) and reduced modulus (E_r) for the H0-H4 samples.

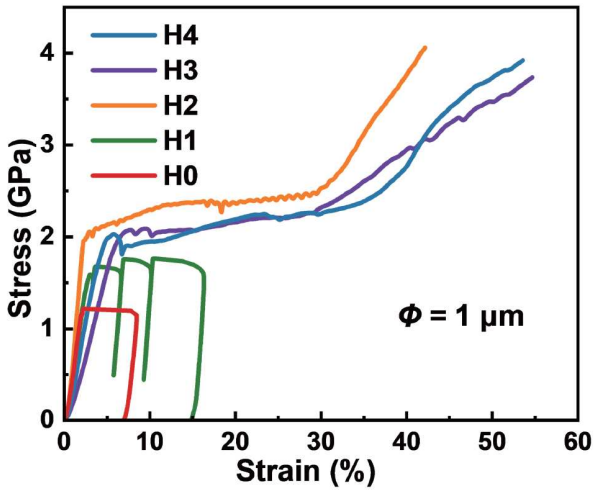

Figure 5 (Color online) Engineering stress-strain curves of the micropillars (1 μm in diameter and 2 μm in height) for the H0-H4 samples.

ges precisely when this interconnected network is fully established. Taken together, Figure 6 demonstrates that a hydrogen content of ⩾1.38 wt.% creates a unique dual-phase architecture that simultaneously delivers superior mechanical performance and a giant magnetocaloric effect. Importantly, in contrast to representative giant magnetocaloric systems like LaFeSi, NiMnCo, and GdSiGe, which tend to be brittle and/or lack sufficient mechanical strength (see Supporting Information Figure S10), the H3 and H4 composites are structurally robust [4,49-52].

The underlying deformation mechanisms for this transition were further revealed by SEM observations of the post-compression surface morphology (Figure 7). For the brittle H0 and H1 samples, the dominant deformation mode is the formation of a single primary shear band along the principal shear plane (Figure 7(a) and Supporting Information Figure S11). Conversely, the marked increase in plasticity for H2-H4 is attributed to the activation and interaction of multiple shear bands. This is evidenced not only by the serrated stress-strain response (Figure 5), which indicates intermittent, distributed slip, but also by direct SEM observations of numerous intersecting shear bands on the deformed micropillars (Figure 7(b)-(d)). The brittle-to-ductile transition can be fundamentally correlated with the formation of a nanometer-scale GdH_2 network. TEM images of compressed pillars (Figure 8) clarify how this nanostructure governs plasticity. In contrast to the H0 sample, which deforms via a single shear band (SB), TEM observations reveal that the H2 and H4 samples exhibit the formation of multiple and interacting SBs, which is characteristic of materials with enhanced plasticity (Figure 8(a)-(c)). Further, it is observed that the HAADF intensity, along with the EDS signals, decreases

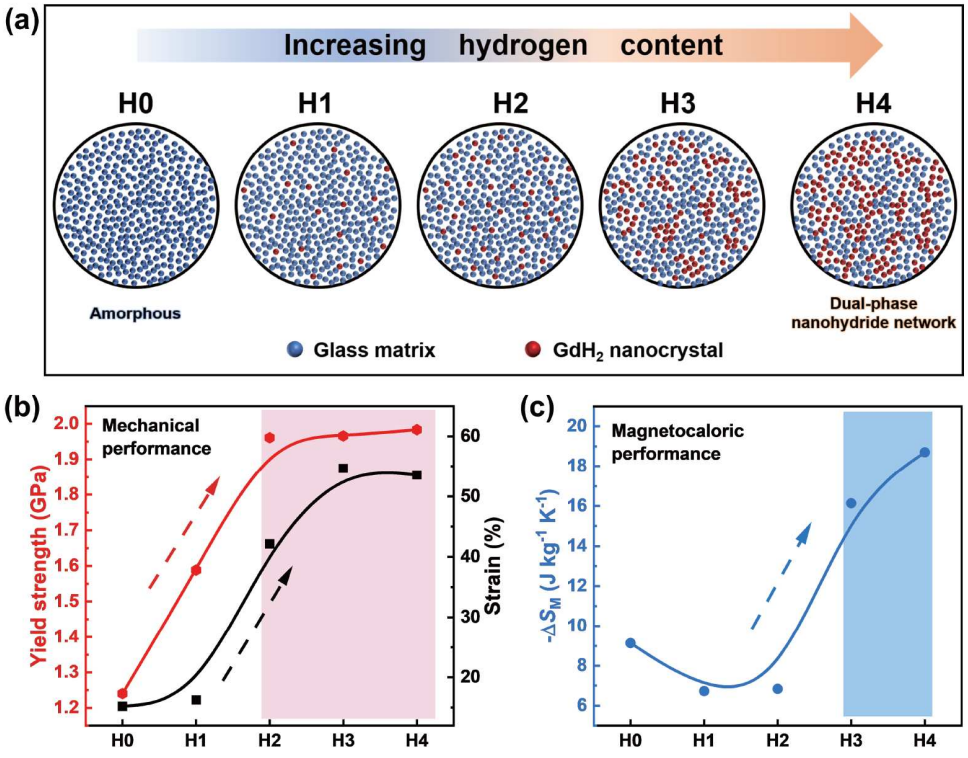

Figure 6 (Color online) Hydrogen-induced microstructural evolution and its effects on mechanical and magnetocaloric performances. (a) Schematic illustration of the hydrogen-induced microstructural evolution, transitioning from a fully amorphous state H0 to an interconnected dual-phase nanohydride network H4. (b) Hydrogen content dependence of the yield strength and compressive strain. (c) Hydrogen content dependence of the $-\Delta S_M^{pk}$ yield strength under a magnetic field change of 5 T.

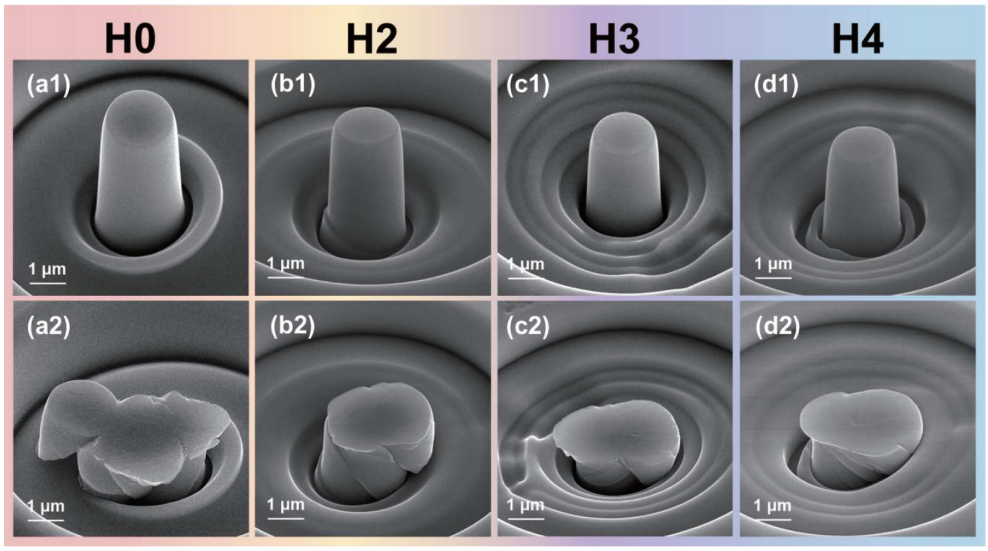

Figure 7 (Color online) Morphological evolution of the micro-pillars before and after compression. (a1)-(d1) SEM images of the H0, H2, H3 and H4 samples (1 μm in diameter) in their as-fabricated state. (a2)-(d2) Corresponding morphologies after compression.

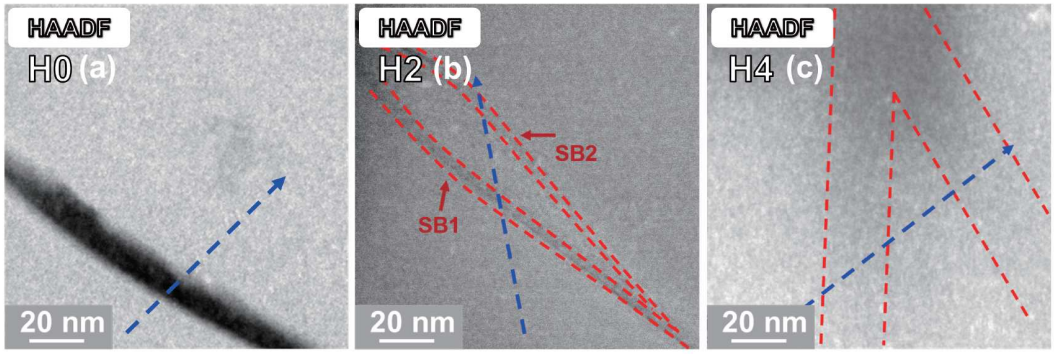

Figure 8 (Color online) Microstructural characterization of the compressed samples. (a)-(c) HRTEM images of the H0, H2, and H4 samples after compression.

significantly across the SB (see Supporting Information Figure S12(a)) in H0, indicating substantial free volume formation. In the hydrogenated samples, this decrease is significantly suppressed (see Supporting Information Figure S12(b) and (c)). Notably, the H2 sample, which possesses the highest compressive strength, exhibits the smallest reduction in HAADF intensity, with drops of 8.1% (from ~27.3 to ~25.1 kCount) at SB1 and 1.9% (from ~26.6 to ~26.1 kCount) at SB2. This trend demonstrates that the GdH_2 nanocrystals effectively limit dilatation, thereby accounting for the highest compressive strength in H2. The H4 sample shows a moderate decrease in signal, consistent with its compressive strength lying between those of H2 and H0. From the above observations, the hydrogen-dependent deformation behavior can be understood as follows. At the low hydrogen level of H1 (~0.39 wt.%), the microstructure contains only sparse 1-2 nm hydride clusters, with typical inter-cluster spacing exceeding 12 nm. Since this spacing surpasses the characteristic STZ diameter (~6 nm) and the volume fraction is well below the percolation threshold, the clusters undergo elastic deformation but fail to generate sufficient secondary shear bands. Consequently, the dominant shear band still propagates almost unimpeded by these hydrides, and thus the measured plastic strain remains unimproved. At hydrogen concentrations between 0.8-1.5 wt.% (H2-H4), the formation of a dense dispersion of closely spaced (2-5 nm) GdH_2 clusters brings each cluster within the stress field of its neighbors, a condition that promotes multiple shear band branching and enables the coupled deformation mechanism described below. Initially, elastic mismatch arises because the shear modulus of GdH_2 is lower than that of the glassy matrix, causing the GdH_2 clusters to yield first and act as compliant inclusions that redistribute stress [53,54]. Subsequently, STZs nucleate more readily at the cluster-glass interface due to its high free volume, promoting the transfer of local strain. Each activated STZ transfers its local strain to neighboring clusters, forcing them to rotate and accommodate the elastic mismatch. This strain

transfer not only facilitates cluster rotation but can also trigger further STZ activation in the surrounding glassy matrix, thereby homogenizing the strain field and preventing localization on a single plane. Ultimately, SB multiplication occurs when the cumulative STZ density reaches a threshold, leading to secondary shear bands branching around the clusters (Figure 8(b) and (c)) [55,56]. This synergistic mechanism in which compliant nanoclusters both initiate and spread plastic strain is the pivotal driver of the hydrogen-induced brittle-to-ductile transition. Given the combination of excellent mechanical robustness and magnetocaloric properties, we anticipate that these dual-phase nanostructured materials hold great promise for cryogenic magnetic refrigeration applications in the 4-20 K range, including hydrogen liquefaction and pre-cooling for quantum computing platforms.

4 Conclusions

We demonstrate that hydrogenation enables nanoscale engineering in a Gd-based AMA, where incremental hydrogen uptake controls the evolution of GdH_2 from sparse 1-2 nm clusters to a network of 2-5 nm nanocrystals in the amorphous matrix. This evolution modulates the mechanical heterogeneity, shifts the magnetic transition from a ferromagnetic to an antiferromagnetic-dominated regime, and alters the critical exponents. Crucially, two distinct hydrogen concentration thresholds governing MCE and mechanical performance are determined. At ~0.83 wt.% H, the critical density of GdH_2 nanocrystals triggers a fundamental transition in deformation mode from isolated obstacle interaction to collective activation of multiple shear bands, thereby abruptly enhancing both strength and plasticity. When the hydrogen content reaches the second threshold (1.38 wt.% H), the GdH_2 nanocrystals form a continuous antiferromagnetic skeleton that quenches long-range ferromagnetic exchange and unlocks a giant MCE. The two sequential thresholds define an optimal property window of hydrogen contents (above 1.38 wt.%), where the unique combination of enhanced multiple shear banding capability and the establishment of a robust antiferromagnetic coupling network collectively delivers excellent magnetocaloric-mechanical synergy. These insights culminate in a targeted material design strategy for engineering next-generation magnetocaloric systems with balanced functional and structural properties.

This work was supported by the National Natural Science Foundation of China (Grant Nos. 52231005 and 51821001).

Conflict of interest The authors declare that they have no conflict of interest.

Supporting Information

The supporting information is available online at http://phys.scichina.com and https://link.springer.com. The supporting materials are published as submitted, without typesetting or editing. The responsibility for scientific accuracy and content remains entirely with the authors.

1 B. G. Shen, J. R. Sun, F. X. Hu, H. W. Zhang, and Z. H. Cheng, Adv. Mater. **21**, 4545 (2009).
2 V. K. Pecharsky, and K. A. Gschneidner, Jr., Phys. Rev. Lett. **78**, 4494 (1997).
3 Y. Shao, J. Liu, M. Zhang, A. Yan, K. P. Skokov, D. Y. Karpenkov, and O. Gutfleisch, Acta Mater. **125**, 506 (2017).
4 L. Miao, X. Lu, Z. Wei, Y. Zhang, Y. Zhang, and J. Liu, Acta Mater. **245**, 118635 (2023).
5 O. Tegus, E. Brück, K. H. J. Buschow, and F. R. de Boer, Nature **415**, 150 (2002).
6 J. Bai, D. Liu, J. Gu, X. Jiang, X. Liang, Z. Guan, Y. Zhang, C. Esling, X. Zhao, and L. Zuo, J. Mater. Sci. Tech. **74**, 46 (2021).
7 J. Lužnik, P. Koželj, S. Vrtnik, A. Jelen, Z. Jagličić, A. Meden, M. Feuerbacher, and J. Dolinšek, Phys. Rev. B **92**, 224201 (2015).
8 T. Gottschall, A. Gràcia-Condal, M. Fries, A. Taubel, L. Pfeuffer, L. Mañosa, A. Planes, K. P. Skokov, and O. Gutfleisch, Nat. Mater. **17**, 929 (2018).
9 J. Lyubina, R. Schäfer, N. Martin, L. Schultz, and O. Gutfleisch, Adv. Mater. **22**, 3735 (2010).
10 Y. Shao, Y. Liu, K. Wang, M. Zhang, and J. Liu, Acta Mater. **195**, 163 (2020).
11 M. Krautz, A. Funk, K. P. Skokov, T. Gottschall, J. Eckert, O. Gutfleisch, and A. Waske, Scripta Mater. **95**, 50 (2015).
12 I. A. Radulov, K. P. Skokov, D. Y. Karpenkov, T. Gottschall, and O. Gutfleisch, J. Magn. Magn. Mater. **396**, 228 (2015).
13 X. C. Zhong, Y. C. Wu, S. M. Wu, Y. X. Li, J. H. Huang, C. L. Liu, H. Zhang, Z. W. Liu, M. L. Zhong, Z. C. Zhong, et al., J. Alloys Compd. **902**, 163780 (2022).
14 Q. Luo, and W. H. Wang, J. Alloys Compd. **495**, 209 (2010).
15 V. Franco, J. S. Blázquez, J. J. Ipus, J. Y. Law, L. M. Moreno-Ramírez, and A. Conde, Prog. Mater. Sci. **93**, 112 (2018).
16 J. Du, Q. Zheng, Y. B. Li, Q. Zhang, D. Li, and Z. D. Zhang, J. Appl. Phys. **103**, 023918 (2008).
17 Y. T. Wang, H. Y. Bai, M. X. Pan, D. Q. Zhao, and W. H. Wang, Sci. China Ser. G-Phys. Mech. As **51**, 337 (2008).
18 H. Fu, and M. Zou, J. Alloys Compd. **509**, 4613 (2011).
19 A. L. Greer, Y. Q. Cheng, and E. Ma, Mater. Sci. Eng.-R-Rep. **74**, 71 (2013).
20 W. Chen, H. Zhou, Z. Liu, J. Ketkaew, N. Li, J. Yurko, N. Hutchinson, H. Gao, and J. Schroers, Scripta Mater. **130**, 152 (2017).
21 Z. Pei, H. Yin, F. Chen, Y. Ma, M. Gao, L. Song, Y. Zhang, W. Xu, J. Q. Wang, and J. Huo, J. Alloys Compd. **1017**, 178974 (2025).
22 Z. Pei, H. Yin, S. Shao, Y. Zhang, M. Gao, L. Song, W. Xu, Y. Tong, X. Jin, J. Xu, et al., J. Non-Cryst. Solids **671**, 123838 (2026).
23 H. Fu, Z. Ma, X. J. Zhang, D. H. Wang, B. H. Teng, and E. Agurgo Balfour, Appl. Phys. Lett. **104**, 072401 (2014).
24 J. Q. Feng, Y. H. Liu, J. H. Sui, A. N. He, W. X. Xia, W. H. Wang, J. Q. Wang, and J. T. Huo, Mater. Today Phys. **21**, 100528 (2021).
25 F. Chen, H. Yin, J. Wang, M. Gao, L. Song, Y. Zhang, W. Xu, C. Zhang, J. Q. Wang, and J. Huo, J. Non-Cryst. Solids **630**, 122893 (2024).
26 H. Yin, J. Y. Law, Y. Huang, H. Shen, S. Jiang, S. Guo, V. Franco, and J. Sun, Sci. China Mater. **65**, 1134 (2022).
27 D. Jia, K. T. Ramesh, and E. Ma, Acta Mater. **51**, 3495 (2003).
28 C. Wang, G. Cao, J. Liu, Y. Zhang, R. Liu, F. Wang, M. Zhang, L. Wang, and B. Zhang, Metals **12**, 1427 (2022).
29 L. Shao, Q. Luo, M. Zhang, L. Xue, J. Cui, Q. Yang, H. Ke, Y. Zhang, B. Shen, and W. Wang, Nat. Commun. **15**, 4159 (2024).
30 Q. Yang, Q. Luo, J. Cui, M. Zhang, H. Chang, H. Zhou, Y. Zhang, and B. Shen, J. Alloys Compd. **1036**, 181964 (2025).
31 L. Shao, L. Xue, Q. Luo, K. Yin, Z. Yuan, M. Zhu, T. Liang, Q. Zeng, L. Sun, and B. Shen, J. Mater. Sci. Tech. **109**, 147 (2022).
32 Q. Zheng, H. Fu, and M. X. Wang, Int. J. Mod. Phys. B **26**, 1250041

(2012).
33 Q. Luo, B. Schwarz, N. Mattern, J. Shen, and J. Eckert, AIP Adv. **3**, 032134 (2013).
34 H. Fu, M. Zou, and N. K. Singh, Appl. Phys. Lett. **97**, 262509 (2010).
35 X. G. Li, T. Otahara, S. Takahashi, T. Shoji, H. M. Kimura, and A. Inoue, J. Alloys Compd. **297**, 303 (2000).
36 W. He, Z. Tang, Q. Gong, M. Yi, and W. Guo, Sci. China-Phys. Mech. Astron. **67**, 226811 (2024).
37 S. P. Mathew, and S. N. Kaul, Appl. Phys. Lett. **98**, 172505 (2011).
38 W. Liu, E. Bykov, S. Taskaev, M. Bogush, V. Khovaylo, N. Fortunato, A. Aubert, H. Zhang, T. Gottschall, J. Wosnitza, et al., Appl. Mater. Today **29**, 101624 (2022).
39 C. R. Muñiz, J. Y. Law, J. Revuelta-Losada, L. M. Ramírez, and V. Franco, Innov. Mater. **1**, 100045 (2023).
40 B. K. Banerjee, Phys. Lett. **12**, 16 (1964).
41 M. E. Fisher, Rep. Prog. Phys. **30**, 615 (1967).
42 A. Arrott, Phys. Rev. **108**, 1394 (1957).
43 J. C. Le Guillou, and J. Zinn-Justin, Phys. Rev. B **21**, 3976 (1980).
44 H. E. Stanley, *Introduction to Phase Transitions and Critical Phenomena* (Oxford University Press, New York, 1971).
45 J. Gong, Z. Mo, Y. Wang, Z. Li, L. Zhang, Q. Fu, Y. Li, and J. Shen, Ceram. Int. **50**, 950 (2024).
46 K. Abdouli, M. Hsini, F. Khammassi, O. Messaoudi, L. Trabelsi, and L. Alfhaid, J. Magn. Magn. Mater. **610**, 172543 (2024).
47 Q. Yang, Q. Luo, J. Cui, B. Sun, F. Hu, Y. Luo, G. Zou, Z. Guo, H. Zhou, M. Zhang, et al., Adv. Funct. Mater. **36**, e29663 (2026).
48 Y. Yang, J. C. Ye, J. Lu, F. X. Liu, and P. K. Liaw, Acta Mater. **57**, 1613 (2009).
49 D. Y. Cong, L. Huang, V. Hardy, D. Bourgault, X. M. Sun, Z. H. Nie, M. G. Wang, Y. Ren, P. Entel, and Y. D. Wang, Acta Mater. **146**, 142 (2018).
50 X. C. Zhong, D. R. Peng, X. T. Dong, J. H. Huang, H. Zhang, Y. L. Huang, S. M. Wu, H. Y. Yu, W. Q. Qiu, Z. W. Liu, et al., Mater. Sci. Eng.-B **263**, 114900 (2021).
51 B. Y. Song, Y. Q. Han, J. Cheng, L. Gao, X. Jin, Z. B. Sun, and J. H. Huang, J. Alloys Compd. **990**, 174398 (2024).
52 S. Sun, J. Bai, J. Gu, K. Guo, N. Morley, Q. Gao, Y. Zhang, C. Esling, X. Zhao, and L. Zuo, J. Alloys Compd. **976**, 173406 (2024).
53 X. Zhou, and C. Chen, Int. J. Plast. **80**, 75 (2016).
54 S. D. Feng, L. Li, K. C. Chan, L. Qi, L. Zhao, L. M. Wang, and R. P. Liu, J. Alloys Compd. **770**, 896 (2019).
55 G. Wu, K. C. Chan, L. Zhu, L. Sun, and J. Lu, Nature **545**, 80 (2017).
56 D. K. Yang, J. T. Wang, D. Fabijanic, P. Cizek, B. S. Li, J. Z. Lu, and P. D. Hodgson, Mater. Sci. Eng.-A **560**, 339 (2013).